




Programming tunable active dynamics in a self-propelled robot

Somnath Paramanick¹, Arnab Pal^{2,3}, Harsh Soni⁴, and Nitin Kumar^{1,a} 

¹ Department of Physics, Indian Institute of Technology Bombay, Powai, Mumbai 400076, India

² The Institute of Mathematical Sciences, CIT Campus, Taramani, Chennai 600113, India

³ Homi Bhabha National Institute, Training School Complex, Anushakti Nagar, Mumbai 400094, India

⁴ School of Physical Sciences, Indian Institute of Technology Mandi, Mandi 175001, India

Received 16 February 2024 / Accepted 28 April 2024

© The Author(s), under exclusive licence to EDP Sciences, SIF and Springer-Verlag GmbH Germany, part of Springer Nature 2024

Abstract We present a scheme for producing tunable active dynamics in a self-propelled robotic device. The robot moves using the differential drive mechanism where two wheels can vary their instantaneous velocities independently. These velocities are calculated by equating robot's equations of motion in two dimensions with well-established active particle models and encoded into the robot's microcontroller. We demonstrate that the robot can depict active Brownian, run and tumble, and Brownian dynamics with a wide range of parameters. The resulting motion analyzed using particle tracking shows excellent agreement with the theoretically predicted trajectories. Later, we show that its motion can be switched between different dynamics using light intensity as an external parameter. Intriguingly, we demonstrate that the robot can efficiently navigate through many obstacles by performing stochastic reorientations driven by the gradient in light intensity towards a desired location, namely the target. This work opens an avenue for designing tunable active systems with the potential of revealing the physics of active matter and its application for bio- and nature-inspired robotics.

1 Introduction

Active matter refers to systems comprised of self-propelled particles that consume energy to perform mechanical work [1–4]. Such systems exhibit striking non-equilibrium phenomena such as collective dynamics, self-organization, and anomalous mechanical properties ubiquitous in the natural and biological world [5–7, 7–17]. Over the past few decades, numerous analytical, numerical, and experimental studies have advanced our understanding of such systems. Yet we are just beginning to realize the potential of active matter in building smart, adaptable materials and autonomous devices [18–20]. Achieving this will require better control over individual particle dynamics and inter-particle interactions. Thus, many studies in recent years have reported concerted efforts to achieve programmable control on active matter spanning a broad range of length scales [21–32]. Here, we develop an active matter system consisting of a collection of smart programmable self-propelled robots capable of sensing their environment using onboard sensors. As a first step, in this paper, we present simple protocols for extracting tunable active dynamics in a single robot.

Previous studies have shown that emerging properties in active systems depend on the self-propulsion

mechanism of individual agents, the strength of alignment interaction, and the nature of the surrounding medium [2]. Therefore, an artificial active material must incorporate all these features to replicate complex non-equilibrium properties displayed by active systems. Yet, broadly speaking, modeling individual constituent dynamics using simple theoretical frameworks of active Brownian particles (ABP) and run-and-tumble particles (RTP) has proven successful in replicating emerging phenomena with great success [3]. Thus, a robotic device, due to its programmability, becomes a natural choice to mimic controlled active particle dynamics. While there are many examples in the literature where robots perform programmable complex self-assembly [33] as well as spontaneous collective behavior [34–37] they rely on vibration motors for locomotion [33–35]. More recently, differential drive robots have also been reported which show much better control of individual dynamics [26, 38–40]. Yet, a detailed protocol to program them with well-established theoretical models of ABP, RTP, and Brownian particle (BP) is missing.

In this work, we present a robotic system that displays a variety of active dynamics with many controllable parameters. Our robot is circularly shaped and propels itself using the differential drive mechanism. In addition, the robot also houses hardware components like multiple infrared (IR) and light intensity

^a e-mail: nkumar@iitb.ac.in (corresponding author)

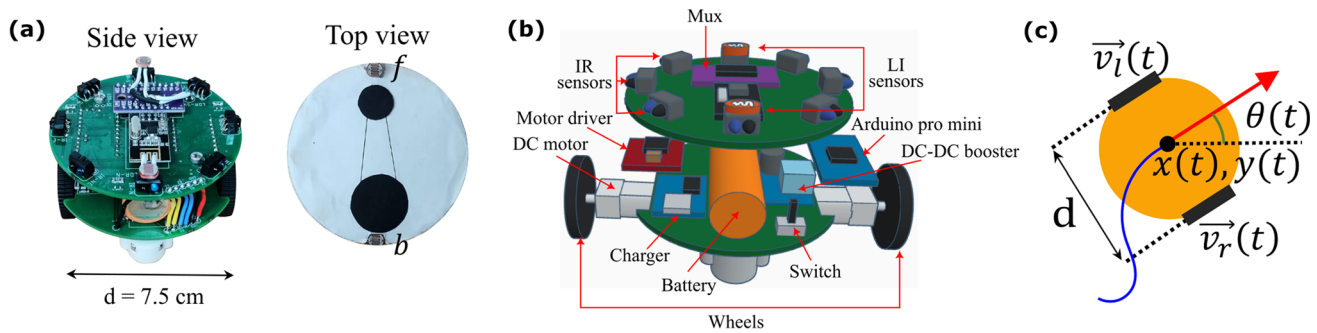


Fig. 1 Robot model: **a** (left) The robot used in the experiment with its diameter indicated. (Right) Top view of the robot with a white paper cap. Two black circles are used to extract the robot's in-plane position coordinates and orientation. f and b represent its front and back LI sensors. **b** An expanded view highlighting the robot's hardware com-

ponents. **c** Robot's position $(x(t), y(t))$ and orientation $\theta(t)$ vary as a function of the instantaneous left and right wheel's velocities ($v_l(t)$ and $v_r(t)$, respectively), resulting in the centre of mass tracing out a trajectory indicated by the blue solid line

(LI) sensors which help it detect environmental factors like obstacles and ambient light. We demonstrate that with its two wheels oppositely placed at a diameter distance away, its center of mass can display a variety of motions depending entirely on the instantaneous wheel velocities. In particular, we show our results on the following three models: (i) Active Brownian particle (ABP) with and without translational noise, (ii) Run and Tumble particle (RTP), and (iii) Brownian particle (BP) dynamics. These results are found to be in excellent agreement with our theoretical modeling. We also show that the robot can be programmed to switch between these dynamics as a function of the ambient light intensity, providing spatiotemporal control over its motion. Finally, we demonstrate the robot's ability to navigate through a complex environment by efficiently avoiding obstacles along its path. We also show that the search time to a desired location can be significantly reduced when we introduce intermittent reorientation of the robot mediated by a smooth external light-intensity gradient.

2 Robot model

Our robot is a circularly shaped electronic gadget with a diameter of 7.5 cm and a height of 5 cm (see Fig. 1a, b). It is assembled using various hardware components as indicated in Fig. 1b. It has two rubber wheels of diameter 3.3 cm placed at the two ends of its diameter. Two caster wheels are placed in the perpendicular direction for support. It also carries eight IR sensors symmetrically placed along the circumference to detect obstacles. Two light intensity (LI) sensors, each placed at the front and back, enable the robot to detect the ambient light intensity gradients. We use the differential drive technique for the robot's movement on a 2D plane surface

by controlling the velocity of the wheels independently [41]. The programs, written using Arduino IDE software, are loaded onto an Arduino pro mini microcontroller board (3.3 V, 8 MHz version), and the output signal is fed to the motor driver (Dual TB6612FNG by SparkFun), that rotates the wheels using two separate DC motors. The signal from the microcontroller provides 256 different analog voltage levels from zero to maximum voltage (5V) to the motors. This gives each wheel a range of velocities, with a maximum of up to 27 cm/sec. All these components are powered using a Li-ion battery. The robot performs its dynamics on a flat surface of dimensions 90 cm \times 120 cm with a white background. We use an overhead projector connected to a computer to illuminate the surface with the desired light intensity. We capture the dynamics of the robot using a high-speed camera from the top and perform image analysis to extract instantaneous position and orientation (see Appendix A).

We begin by writing the equations of motion of the robot in two dimensions. Let $v_l(t)$ and $v_r(t)$ be the velocities of the left and right wheels of the robot along its orientation at time t (see Fig. 1c). Then, the equations of motion for the instantaneous position $(x(t), y(t))$ and the orientation angle $\theta(t)$ of the robot read

$$\begin{aligned}\dot{x}(t) &= \frac{v_l(t) + v_r(t)}{2} \cos \theta(t), \\ \dot{y}(t) &= \frac{v_l(t) + v_r(t)}{2} \sin \theta(t), \\ \dot{\theta}(t) &= \frac{v_r(t) - v_l(t)}{d},\end{aligned}\quad (1)$$

where d is the diameter of the robot, and the dot stands for the time derivative. We next show that purely based on the instantaneous values of v_l and v_r , we can program the robot to perform desired stochastic dynamics.

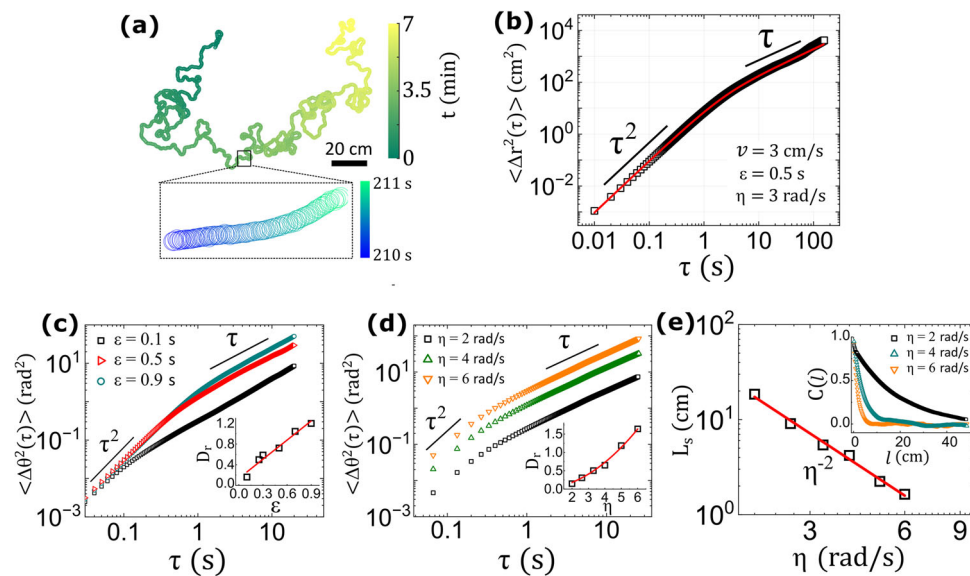


Fig. 2 ABP model without translational noise: **a** A typical trajectory of the robot following ABP dynamics with velocity $v = 3$ cm/s, delay time $\epsilon = 0.5$ s, and rotational noise $\eta = 3$ rad/s. The color bar represents the time. The zoomed-in portion of the trajectory shows the robot moving with a constant velocity at all time steps, indicative of the absence of translational noise at short time scales. **b** Translational mean-square displacement (MSD) of the trajectory plotted as a function of time τ showing a ballistic ($\sim \tau^2$) to diffusive ($\sim \tau$) transition. The solid line shows the fit with the analytical expression given by (4). **c** Angular MSD, $\langle \Delta\theta^2(\tau) \rangle$, plotted for three values of ϵ keeping

$\eta = 3$ rad/s. $\langle \Delta\theta^2(\tau) \rangle$ also undergoes a ballistic to diffusive transition at time ϵ . (Inset) The experimental values of D_r , measured by line fitting the linear part of the MSD, show linear scaling with ϵ . **d** Angular MSD as a function of τ for different values of η keeping ϵ fixed at 0.25 s. (Inset) D_r extracted from the plots increases quadratically with η . **e** Persistence length L_s shows an algebraic decay with η with an exponent consistent with theory. L_s is extracted by fitting an exponential function to the spatial velocity autocorrelation function, $C(l) = \langle \mathbf{v}(r) \cdot \mathbf{v}(r+l) \rangle_r / \mathbf{v}^2$ shown in the inset

3 Results and discussion

3.1 ABP model without translational noise

A distinctive feature of a polar active particle is its finite self-propulsion speed. In general, it can have rotational as well as translational noise. We first study the case without an explicit source of translational noise. In that case, it is often modeled as an ABP, which is equivalent to a biased random walk in two dimensions where the particle always moves in the direction of its instantaneous orientation. Consequently, the ABP moves with a constant speed but its direction changes randomly in the plane. The dynamics of an ABP of speed v is governed by the following equations of motion:

$$\begin{aligned}\dot{x}(t) &= v \cos \theta(t), \\ \dot{y}(t) &= v \sin \theta(t), \\ \dot{\theta}(t) &= \zeta(t),\end{aligned}\quad (2)$$

where ζ is the instantaneous rotational speed of the ABP; it is a white noise with a zero mean and is often modeled as white Gaussian noise. We compare (2) and (1) to obtain the expressions of v_l and v_r , which yields

$$\begin{aligned}v_l(t) &= \frac{2v + \zeta(t)d}{2}, \\ v_r(t) &= \frac{2v - \zeta(t)d}{2}.\end{aligned}\quad (3)$$

where $v = (v_l(t) + v_r(t))/2$ is the instantaneous in-plane speed which is constant. $\zeta(t) = (v_r(t) - v_l(t))/d$ is the instantaneous rotational speed. To mimic ABP motion, the values of $v_l(t)$ and $v_r(t)$ are updated in the robot such that v remains constant and the value of ζ is updated discretely from a uniform distribution between $[-\eta, \eta]$ after every ϵ seconds, termed as delay time. Note that we have used uniform distribution instead of white Gaussian noise. This changes the robot's motion in short time scale but eventually is the same as the Gaussian model at a larger time. In experiments, the accessible values of parameters η and ϵ lie between 1–6 rad/s and 0.1–0.9 s, respectively.

When implemented in the robot, it mimics the ABP motion quite well. A typical trajectory of the robot is shown in Fig. 2a and SI movie S1. We do our experiment in a confined arena. But to get unbounded free particle trajectory, we use boundary wall detection using IR sensors to remove the confinement effects (see Appendix B). The zoomed-in part of the trajectory ascertains the absence of translational noise at short time scales. The mean squared displacement (MSD) shows a transition from ballistic to diffusive behavior, a hallmark feature

of the ABP dynamics (see Fig. 2b). Using a simple theoretical calculation, we obtain the following expression for the MSD [42, 43]

$$\langle \Delta r^2(\tau) \rangle = \frac{2v^2}{D_r} \left[\tau + \frac{1}{D_r} (e^{-D_r \tau} - 1) \right], \quad (4)$$

where $D_r = \epsilon \langle \zeta^2 \rangle / 2 = \epsilon \eta^2 / 6$ (see Appendix C). The solid red line in Fig. 2b represents analytically obtained MSD, which shows an excellent agreement with our experimental data. We further plot angular MSD defined as $\langle \Delta \theta^2(\tau) \rangle$ for varying ϵ and η independently (see Fig. 2c, d). Interestingly, we find that $\langle \Delta \theta^2(\tau) \rangle$ scales linearly with τ only for $\tau > \epsilon$, whereas for $\tau < \epsilon$, the plot is ballistic with τ^2 scaling. This happens because during the time duration ϵ , the robot always rotates with a constant angular velocity of magnitude $|(v_l - v_r)/d|$, resulting in $\Delta \theta$ scaling linearly with τ . For given ϵ and η , the experimental value of D_r is measured by line-fitting $\langle \Delta \theta^2(\tau) \rangle$, using the formula $\langle \Delta \theta^2(\tau) \rangle = 2D_r \tau$. We then plot D_r as a function of ϵ and η in the insets of Fig. 2c, d, respectively, showing D_r indeed scaling according to the expression $D_r = \epsilon \eta^2 / 6$, as predicted by the theory.

We also measure spatial velocity autocorrelation function, $C(l) = \langle \mathbf{v}(r) \cdot \mathbf{v}(r+l) \rangle_r / v^2$, where r is the distance traveled by the robot, with respect to l for different values of η keeping ϵ constant at 0.25 s as shown in Fig. 2e inset. We find that $C(l) \propto e^{-l/L_s}$, where L_s is the persistence length. Using the above relation, we extracted L_s for different η . We find that L_s decreases algebraically with η with an exponent of “-2”. This also agrees with the theory since $L_s = v/D_r \propto \eta^{-2}$.

3.2 ABP model with translational noise

In general, at small time scales, a polar particle may have translational noise along as well as normal to its orientation. In this case, therefore, v in (2) is not a constant and rather fluctuates around its mean value. We achieve this by generating $v_l(t)$ and $v_r(t)$ from two statistically independent random uniform distributions in a range of $2V$ with a finite mean v_a , i.e., in the interval $[v_a - V, v_a + V]$. Here V quantifies the strength of the translational noise. Interestingly, since our robot can only move along the direction of its wheels at any instance, this noise features only in the velocity component, which is parallel to its orientation, while noise normal to its orientation is forbidden. As a result, both $\dot{\theta}(t) = (v_r(t) - v_l(t))/d$ and $v(t) = (v_l(t) + v_r(t))/2$ become random variables with zero and a non-zero mean ($= v_a$), respectively. Similar to the previous model the values of v_l and v_r are discretely updated after every ϵ seconds in the robot.

Figure 3a and SI movie S2 show a typical trajectory of the robot following noisy ABP dynamics. At long time scales, the trajectory qualitatively looks similar to the ABP without translational noise shown in Fig. 2b but differs significantly at short time scales

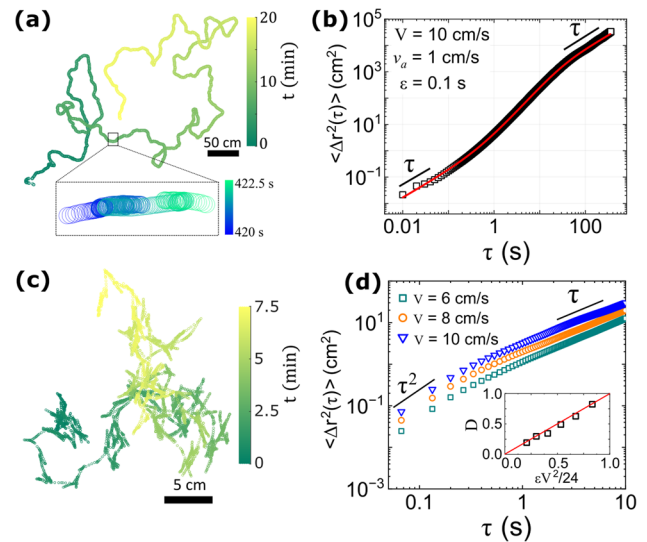


Fig. 3 ABP model with translational noise and BP model: **a** Typical trajectory of the robot programmed to follow ABP model with translational noise having $V = 10$ cm/s, $\epsilon = 0.1$ s, and $v_a = 1$ cm/s. The color bar represents the time. The zoomed-in trajectory shows the presence of translational noise in the form of significant back-and-forth events along the robot's orientation. **b** The translational MSD shows a diffusive to super-diffusive to diffusive transition as a function of time. The solid line is fit with the analytical expression given by (5). **c** A typical trajectory of the robot following a BP motion with $V = 7$ cm/s, $\epsilon = 0.2$ s, and $v_a = 0$ cm/s. The color bar represents the time of motion. **d** The translational MSD of the BP motion plotted for three values of V keeping ϵ fixed at 0.2 s shows a ballistic to diffusive transition. The ballistic motion is a consequence of the finite delay time ϵ which also sets the crossover time for all the curves. The inset shows the diffusion constant D measured from the MSD curves matches with $\epsilon V^2 / 24$ as predicted by the theory

as depicted by frequent back-and-forth events in the zoomed-in trajectory. We plot experimentally measured MSD in Fig. 3b, which shows scaling with τ at both short and very long time scales as reported in past studies [43, 44]. We solve the Langevin equation for this case and obtain the following expression of the MSD

$$\langle \Delta r^2(\tau) \rangle = 4D_t \tau + \frac{2v_a^2}{D_r^2} [D_r \tau + (e^{-D_r \tau} - 1)], \quad (5)$$

where $D_t = \epsilon V^2 / 24$ and $D_r = \epsilon V^2 / 3d^2$ are the translational and the rotational diffusion constants, respectively (see Appendix C for theoretical calculation). Again the experimental data agree well with the analytical MSD expression (solid red line) over the entire range of time scales (Fig. 3b). It is worth noting that the system has two distinct time scales: one associated with the rotational diffusion $1/D_r$ and the other one associated with the translational noise i.e., D_t/v_a^2 . It turns out that one should have $1/D_r \gg D_t/v_a^2$ within the relevant experimental parameters in our

setup. With this knowledge, we can try to probe different behaviors in the MSD that emanate from these timescales. For instance, when $\tau \gg 1/D_r$ one finds $\langle \Delta r^2(\tau) \rangle_{\tau \gg 1/D_r} \approx 4[D_t + v_a^2/(2D_r)]\tau$ – a linear relation in τ . In the intermediate time scale $D_t/v_a^2 \ll \tau \ll 1/D_r$, we find $\langle \Delta r^2(\tau) \rangle_{D_t/v_a^2 \ll \tau \ll 1/D_r} \approx v_a^2 \tau^2$ – a ballistic scaling. Finally, in the shortest time scale $\tau \ll D_t/v_a^2$, we again observe the diffusive scaling, i.e., $\langle \Delta r^2(\tau) \rangle_{\tau \ll D_t/v_a^2 \ll 1/D_r} \approx 4D_t\tau$. These behaviors show an excellent agreement with our experimental results.

3.3 Brownian particle model

A Brownian particle (BP) in two dimensions can move in any direction with an equal probability. However, quite obviously, the wheels of our robot can move only along its direction of orientation, not normal to it. Here we show that it is possible for our robot to perform BP dynamics with limited movement of its wheels. Notably, the ABP motion with noise described in the previous section reduces to the BP dynamics when $v_a = 0$. As a result, both $v(t)$ and $\dot{\theta}$ become random variables with zero mean. Figure 3c and SI movie S3 show the trajectory of the robot following the BP model with $V = 7$ cm/s and $\epsilon = 0.2$ s. The resulting MSD shows that at short times ($< \epsilon$) the motion is ballistic, and at longer times, it is diffusive (see Fig. 3d), similar to $\langle \Delta \theta^2(\tau) \rangle$ observed in Fig. 2c, d. Again, the ballistic regime is a consequence of finite velocity events experienced by both left and right wheels over a time interval of ϵ as both v_l and v_r are updated discretely after every ϵ second. This is further verified by the fact that the crossover from ballistic to diffusive regime happens exactly after ϵ second.

Moreover, since $\langle \Delta r^2(\tau) \rangle = 4D\tau$, we extract the diffusion constants D from the MSD plots for various values of V and ϵ . We plot this value with the analytical result (see Appendix C), which predicts $D = \epsilon \langle v^2 \rangle / 4 = \epsilon V^2 / 24$ in Fig. 3d inset. Clearly, we find an excellent agreement with the theory (solid line indicating the equality).

3.4 Run and tumble particle model

We now turn our attention to the RTP models, where an individual particle moves in a straight line interrupted by frequent tumble events that randomize its run direction (Fig. 4a) [45, 46]. Such motion is widely observed in micro-organisms like bacteria [47] and even in active granular particles [48]. In the case of our robot, it runs when the left and right wheels have the same velocities, i.e., $v_l = v_r = v_{\text{run}}$, and it tumbles to a new direction when $v_l = -v_r$. A typical trajectory of the robot performing RTP motion is shown in Fig. 4b and SI movie S4 with its instantaneous speed plotted in Fig. 4c. Here, the robot runs with a constant speed v_{run} for a duration τ_r (run time), after which it tumbles over a time τ_t (tumble duration). It is important to highlight that τ_t can never be zero in our experiments, and indeed

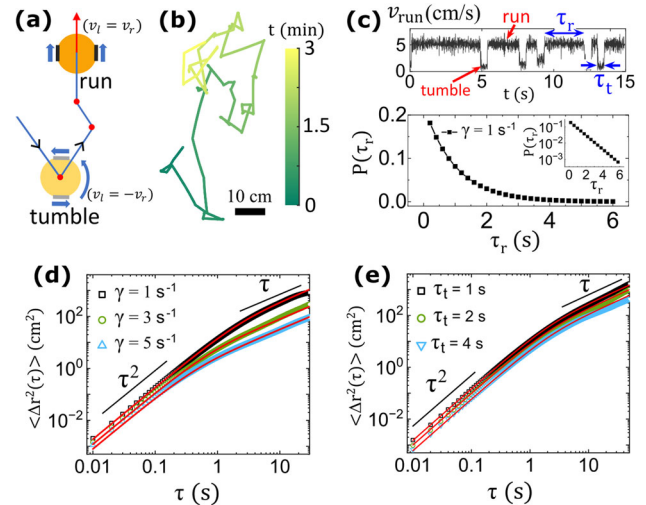


Fig. 4 RTP model: **a** A typical schematic of the robot mimicking RTP model. A run event is characterized by a straight trajectory when $v_l = v_r$. The robot tumbles while $v_l = -v_r$ and finds a new run direction randomly. **b** The trajectory of the robot for a duration of 3 min, programmed to follow RTP model. The color bar shows the time. **c** The top plot shows the instantaneous speed of the robot, which switches between $v_{\text{run}} = 5$ cm/s and $v_{\text{run}} = 0$, representing run and tumble, respectively. τ_r and τ_t represent run and tumble duration, respectively. τ_t is constant during the motion, whereas τ_r is extracted from an exponential distribution $P(\tau_r) = \gamma e^{-\gamma \tau_r}$ as shown in the bottom plot. A linear semi-log plot in the inset verifies the exponential distribution. Parameter values for the trajectory shown in (b) are $v_{\text{run}} = 5$ cm/s, $\gamma = 3$ s $^{-1}$, and $\tau_t = 0.5$ s. **d** Translational MSD as a function of time for three different γ values keeping $\tau_t = 0.5$ s. Solid pink lines are the fit with the theoretical expression given by (6). **e** Translational MSD for three different τ_t values keeping the τ_r distribution fixed with $\gamma = 1$ s $^{-1}$. Again, solid lines represent the fit with the same theoretical expression

in any experiment, since the robot can never tumble instantaneously. Inspired by the experimental observations in bacteria [47], we choose τ_r from an exponential distribution $P(\tau_r) = \gamma e^{-\gamma \tau_r}$, whereas τ_t is kept constant for all tumble events. This is achieved by scaling the tumble speed with the tumble angle, which is chosen randomly between 0 and 360 degrees. The RTP trajectory shown in Fig. 4b has $v_{\text{run}} = 5$ cm/s, $\gamma = 3$ s $^{-1}$, and $\tau_t = 0.5$ s. Later, we perform experiments for various τ_r distributions characterized by γ at fixed $\tau_t = 0.5$ s. The resulting MSD is shown in Fig. 4d, showing a ballistic ($\sim \tau^2$) to diffusive ($\sim \tau$) transition with transition time decreasing as we increase γ . However, when we vary τ_t while keeping γ constant (Fig. 4e for $\gamma = 1$ s $^{-1}$), the transition time remains independent of τ_t . Regardless, the MSD measured experimentally shows an excellent agreement with the theoretical expression given by [49]

$$\langle \Delta r^2(\tau) \rangle = \frac{1}{1 + \gamma \tau_t} \frac{2v_{\text{run}}^2}{\gamma^2} (\gamma \tau - 1 + e^{-\gamma \tau}). \quad (6)$$

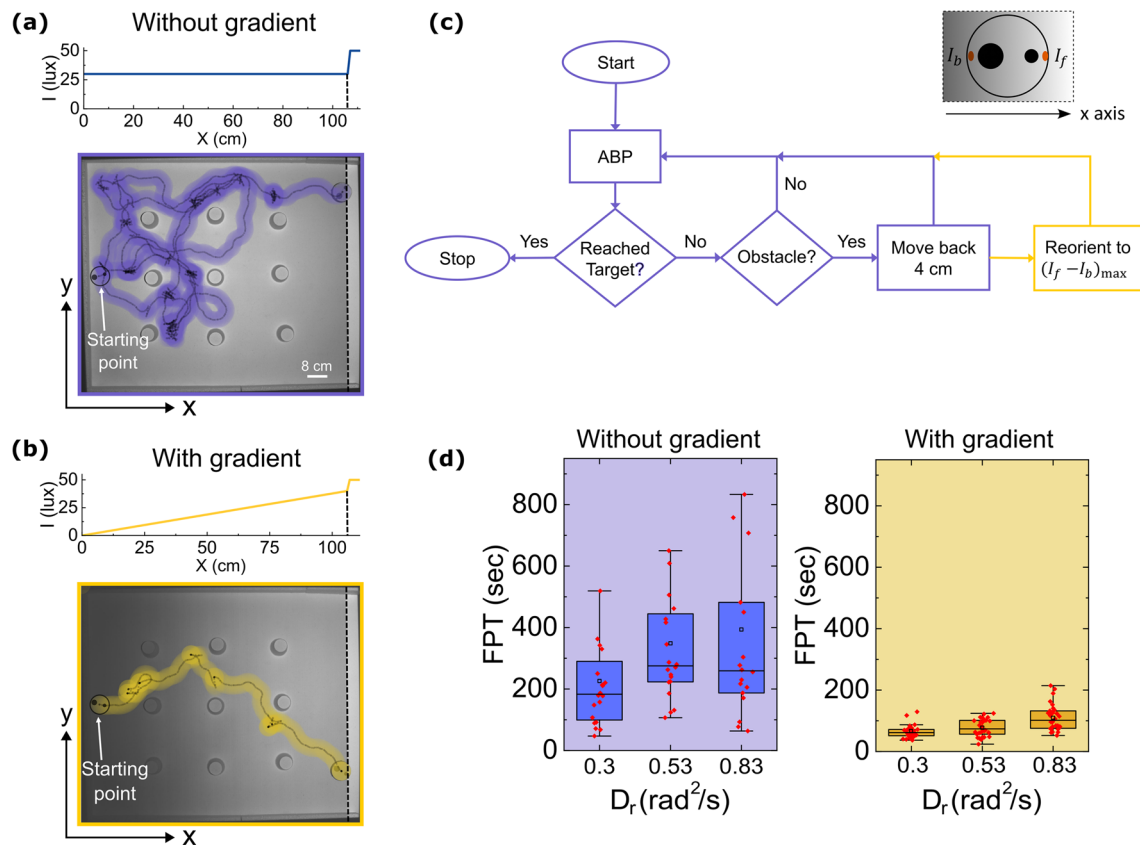


Fig. 5 Navigating through obstacles: **a** (Top) Without the light-gradient, the intensity is kept uniform along the horizontal direction (x -axis). The target region is denoted as the brightest region. (Bottom) A typical trajectory of the robot navigating while avoiding obstacles to reach the target. The centre of mass (COM) traces the solid line, whereas the shaded region marks the robot's body. **b** (Top) In the case of an external light gradient, the intensity increases linearly as a function of x . (Bottom) A typical path followed by the robot in the presence of light gradient-mediated reorientation. **c** The algorithm encoded into the robot shown in the

form of a flowchart. An additional set of instructions shown in yellow are followed in the presence of the light gradient. (Inset) I_f and I_b respectively represent intensity readings at the robot's front and back LI sensors. $(I_f - I_b)$ is the maximum when the robot's orientation is parallel to the x -axis i.e., towards the target. **d** Box plot of first passage time (FPT) for both with and without light gradient cases. FPT is significantly higher in the absence of a light gradient than in the case with light gradient-mediated reorientations for three typical values of D_r .

The solid red lines in Fig. 4d, e show the fit, which is in excellent agreement with the experimental results.

3.5 Light-activated dynamics

Here, we show that the robot can be programmed to switch between the various dynamics discussed above using light intensity as an external parameter. Since our robot is equipped with two LI sensors at its front and back (Fig. 1a, b) it continuously measures the value of ambient light intensity, which is set using the overhead projector. We load multiple programs onto the robot's microcontroller and assign light intensity values for each program. For example, we can program the robot to display ABP dynamics when the measured light intensity is between $I_1 - I_2$, BP between $I_3 - I_4$, etc., where I_1 , I_2 , I_3 & I_4 are arbitrary. We summarize this result in SI movie S5, where a robot is programmed to display

BP, ABP, and RTP motion as a function of increasing light intensity.

3.6 Demonstration of obstacle sensing for efficient navigation

In conjunction with the above-mentioned dynamics, our robot also has a unique ability to navigate efficiently through obstacles. In this section, we demonstrate how the robot can sidestep physical obstacles, consequently speeding up the efficiency of locating desired targets. To this end, we intend our robot to traverse an area containing multiple physical obstacles consisting of paper cups (see Fig. 5a). The starting point is positioned midway along the left edge, with the objective of reaching a point on the right edge, marked by a dashed black line, at a distance of 106 cm. Our strategy involves leveraging an external light gradient to aid navigation, enabling

the robot to promptly reorient itself towards the target whenever obstacles are detected.

Therefore, we conduct two sets of experiments: one with uniform illumination across the area and another with an external light gradient along the horizontal axis (refer to Fig. 5a, b). The corresponding spatial light intensity distributions are depicted in Fig. 5a, b. Note that there is no gradient in the y-direction. In both scenarios, the robot is programmed to follow the ABP model (as discussed in Sect. 3.1) with $v = 5$ cm/s. Once the robot reaches the target location, the corresponding stochastic time is noted as the first passage time (FPT) for that realization. Figure 5c shows the algorithm programmed into the robot for executing this task. Along its path, whenever the robot is within a distance of 1 cm from an obstacle or the boundary wall, one of its eight IR sensors gets activated and retracts backward by 4 cm in a straight line. Thus, the robot never directly hits the obstacles.

In the first case when the light gradient is absent (see Fig. 5a), the robot restarts the ABP motion in a random direction after retraction. However, in the case with a light gradient, it reorients to a direction that maximizes the difference in front and back LI sensor readings ($I_f - I_b$) and restarts the ABP motion (Fig. 5c inset). Simply put, by design, the robot reorients towards the target before restarting its ABP motion, which is the area with the highest intensity (Fig. 5b). The typical trajectories traversed by the robot in two scenarios are shown in Fig. 5a, b respectively and SI Movie S6. As a result, we find that the navigation time measured in terms of FPT for three values of D_r is significantly lower for the case with the light gradient than without it (see Fig. 5d). This demonstration emphasizes our robot's ability to effectively navigate a complex landscape of obstacles by leveraging its obstacle and light-sensing capabilities.

4 Conclusion

Here, we introduced an experimental system consisting of self-propelled robots. The robots are electronic devices capable of executing a preloaded program and simulating it to in-plane dynamics with excellent control. Using hardware components like IR and LI sensors, they can also detect obstacles and ambient light intensity and modify their motion as required. The robots are driven by two wheels placed diametrically opposite to each other and move independently with velocities v_l and v_r , respectively. We first show that instantaneous values of v_l and v_r calculated from scalar active particle models like Active Brownian, Run and Tumble, and Brownian motion reproduce desired stochastic dynamics in the centre of mass of the robots quite accurately. The experimental parameter space over which this motion can be tuned is quite exhaustive and highly tunable. We demonstrated the control over robot motion using ambient light as an external control parameter. For instance, the robot can interact with an external light intensity *gradient*, which can significantly reduce

the navigation time. Lastly, we showed that the robot can effectively detect and avoid obstacles while navigating a complex environment. Overall, the experimental system presented in this paper holds potential in unraveling laws governing the non-equilibrium physics of active and living systems with applications to smart and adaptive material design.

Supplementary information The online version contains supplementary material available at <https://doi.org/10.1140/epje/s10189-024-00430-x>.

Acknowledgements NK acknowledges financial support from DST-SERB for CRG grant number CRG/2020/002925 and IITB for the seed grant. NK also thanks Sriram Ramaswamy and Sanjib Shabhapanidit for productive discussions. AP acknowledges research support from the DST-SERB Start-up Research Grant Number SRG/2022/000080 and the Department of Atomic Energy, India. HS acknowledges SERB for the SRG (Grant No. SRG/2022/000061-G). SP thanks CSIR India for research fellowship.

Author contribution statement

SP designed and developed the robot. SP and NK designed the experimental models. HS and AP did the theoretical calculations. All authors contributed equally in drafting the paper.

Data availability This manuscript has associated data in a data repository. [Authors' comment: The authors declare that the data associated with this study is already in the paper. The detailed datasets generated during the current study are available from the corresponding author on reasonable request.]

Appendix A: Image-analysis technique

In experiments on modeling the robot dynamics, we cover the robot's components (except the light intensity sensors) with a white paper cap with two black circles drawn on top of it, one bigger than the other, along the robot's orientation. We then use in-house MATLAB code to extract the circles' position coordinates. The vector connecting the circles provides the instantaneous orientation of the robot, and the midpoint of the line connecting them provides the center-of-mass coordinate. The frame rate at which movies are captured varies between 10 and 100 depending on the robot's speed. The movies are captured for a duration of 1 h for each model.

Appendix B: Removing confinement effect

Theoretical models of ABP, RTP, and BP dynamics consider an unbounded motion of the particle. In our experiments, we use the following protocol to remove confinement effects caused by boundary walls. Once the robot detects

the boundary through its IR sensors, it moves 40 cm in the reverse direction while maintaining its orientation. Later, we remove these straight trajectories from the experiments and stitch all the stochastic tracks together by shifting the coordinates appropriately. This creates a continuous free particle motion that is effectively unconfined.

Appendix C: Theoretical calculation

C.1 ABP model without translational noise

In general, the equations of motion for the robot are given by

$$\dot{x}(t) = v(t) \cos \theta(t), \quad (\text{C1a})$$

$$\dot{y}(t) = v(t) \sin \theta(t), \quad (\text{C1b})$$

$$\dot{\theta}(t) = \zeta(t), \quad (\text{C1c})$$

where $v(t)$ is the component of the instantaneous robot velocity along its orientation $\mathbf{n} = (\cos \theta(t), \sin \theta(t))$. The values of v and ζ are varied discretely with the step size of ϵ second. For mimicking the ABP model, v is kept constant and $\zeta(t)$ is chosen to be a random number with a uniform distribution between $[-\eta, \eta]$. For the time scales much larger than ϵ ,

$$\langle \zeta(t) \zeta(t') \rangle = 2D_r \delta(t - t'), \quad (\text{C2})$$

where D_r is the rotational diffusion constant. It is straightforward to show that [50]

$$\langle [\theta(\tau) - \theta(0)]^2 \rangle = 2D_r \tau. \quad (\text{C3})$$

Here the angular bracket represents the ensemble average. Whereas, from the discrete form of (C1c),

$$\theta(\tau) = \theta(0) + \epsilon \sum_{i=1}^{N_\tau} \zeta_i, \quad (\text{C4})$$

where $\zeta_i \equiv \zeta(i\epsilon)$ and $N_\tau = \tau/\epsilon$. As the random number ζ_i has the uniform probability distribution between $[-\eta, \eta]$,

$$\langle \zeta_i \zeta_j \rangle = \delta_{ij} \frac{\eta^2}{3}. \quad (\text{C5})$$

Then, from (C4),

$$\begin{aligned} \langle [\theta(\tau) - \theta(0)]^2 \rangle &= \epsilon^2 \sum_{i=1}^{N_\tau} \sum_{j=1}^{N_\tau} \langle \zeta_i \zeta_j \rangle \\ &= \epsilon^2 \sum_{i=1}^{N_\tau} \langle \zeta_i^2 \rangle \\ &= \epsilon^2 N_\tau \frac{\eta^2}{3} \\ &= \epsilon \tau \frac{\eta^2}{3} \end{aligned} \quad (\text{C6})$$

Comparing the above equation with (C3), we obtain

$$D_r = \epsilon \frac{\eta^2}{6}. \quad (\text{C7})$$

C.2 ABP with translational noise

In this case, $v(t)$ in (C1) is not constant, it rather fluctuates around its mean value. The values of $v(t)$ and $\zeta(t)$ in terms of the velocities of the left and right wheels of the robot, v_l and v_r , are given by

$$v(t) = \frac{v_r(t) + v_l(t)}{2}, \quad (\text{C8a})$$

$$\zeta(t) = \frac{v_r(t) - v_l(t)}{d}, \quad (\text{C8b})$$

where d is the diameter of the robot. Here v_l and v_r are statistically independent random numbers with a uniform probability distribution in the range $[v_a - V, v_a + V]$. Then, one can readily show that

$$\langle v_r(i\epsilon) v_r(j\epsilon) \rangle = \delta_{ij} \frac{V^2}{3} + v_a^2, \quad (\text{C9})$$

$$\langle v_l(i\epsilon) v_l(j\epsilon) \rangle = \delta_{ij} \frac{V^2}{3} + v_a^2, \quad (\text{C10})$$

$$\langle v_r(i\epsilon) v_l(j\epsilon) \rangle = 0. \quad (\text{C11})$$

Then the relations (C8) give

$$\langle v(i\epsilon) v(j\epsilon) \rangle = \delta_{ij} \frac{V^2}{6} + v_a^2, \quad (\text{C12})$$

$$\langle \zeta(i\epsilon) \zeta(j\epsilon) \rangle = \delta_{ij} \frac{2V^2}{3d^2}, \quad (\text{C13})$$

$$\langle v(i\epsilon) \zeta(j\epsilon) \rangle = 0. \quad (\text{C14})$$

For the time scales much larger than ϵ , it is obvious from (C12) that

$$\langle v(t) v(t') \rangle = 4D_t \delta(t - t') + v_a^2, \quad (\text{C15})$$

and ζ follows the correlation relation given by (C2). Following the similar steps as done in Sect. C.1, one can show that

$$D_r = \frac{\epsilon V^2}{3d^2}, \quad (\text{C16})$$

$$D_t = \frac{\epsilon V^2}{24}. \quad (\text{C17})$$

The mean square displacement can then be calculated as follows

$$\begin{aligned} \Delta r^2(\tau) &= \langle [\mathbf{r}(\tau) - \mathbf{r}(0)] \cdot [\mathbf{r}(\tau) - \mathbf{r}(0)] \rangle \\ &= \left\langle \int_0^\tau dt \int_0^\tau dt' v(t) v(t') \cos [\theta(t) - \theta(t')] \right\rangle \\ &= \int_0^\tau dt \int_0^\tau dt' \langle v(t) v(t') \cos [\theta(t) - \theta(t')] \rangle. \end{aligned} \quad (\text{C18})$$

As v and ζ are statistically independent of each other [from (C14)], we have

$$\Delta r^2(\tau) = \int_0^\tau dt \int_0^\tau dt' \langle v(t) v(t') \rangle \langle \cos [\theta(t) - \theta(t')] \rangle.$$

Using (C15) and the following relation [42, 51–54]

$$\langle \cos [\theta(t) - \theta(t')] \rangle = \exp(-D_r |t - t'|), \quad (\text{C19})$$

we arrive at

$$\begin{aligned}\Delta r^2(\tau) &= \int_0^\tau dt \int_0^\tau dt' \left\{ [4D_t \delta(t-t') + v_a^2] \right. \\ &\quad \times \exp(-D_r |t-t'|) \left. \right\} \\ &= 4D_t \tau + \frac{2v_a^2}{D_r^2} \left[D_r \tau + (e^{-D_r \tau} - 1) \right],\end{aligned}\quad (\text{C20})$$

which was used in Eq. (5). To imitate the BP model, we set $v_a = 0$ to obtain

$$\Delta r^2(\tau) = 4D_t \tau. \quad (\text{C21})$$

Note that here the dynamics of the robot does not depend on the rotational diffusion constant D_r .

References

1. S. Ramaswamy, The mechanics and statistics of active matter. *Annu. Rev. Condens. Matter Phys.* **1**, 323 (2010)
2. M.C. Marchetti, J.-F. Joanny, S. Ramaswamy, T.B. Liverpool, J. Prost, M. Rao, R.A. Simha, Hydrodynamics of soft active matter. *Rev. Mod. Phys.* **85**, 1143 (2013)
3. H. Chaté, Dry aligning dilute active matter. *Annu. Rev. Condens. Matter Phys.* **11**, 189 (2020)
4. J. Toner, Y. Tu, S. Ramaswamy, Hydrodynamics and phases of flocks. *Ann. Phys.* **318**, 170 (2005)
5. N. Kumar, H. Soni, S. Ramaswamy, A. Sood, Flocking at a distance in active granular matter. *Nat. Commun.* **5**, 4688 (2014)
6. T. Sanchez, D.T. Chen, S.J. DeCamp, M. Heymann, Z. Dogic, Spontaneous motion in hierarchically assembled active matter. *Nature* **491**, 431 (2012)
7. J. Brugués, D. Needleman, Physical basis of spindle self-organization. *Proc. Natl. Acad. Sci.* **111**, 18496 (2014)
8. M.E. Cates, J. Tailleur, Motility-induced phase separation. *Annu. Rev. Condens. Matter Phys.* **6**, 219 (2015)
9. N. Kumar, R. Zhang, S.A. Redford, J.J. de Pablo, M.L. Gardel, Catapulting of topological defects through elasticity bands in active nematics. *Soft Matter* **18**, 5271 (2022)
10. J. Palacci, S. Sacanna, A.P. Steinberg, D.J. Pine, P.M. Chaikin, Living crystals of light-activated colloidal surfers. *Science* **339**, 936 (2013)
11. N. Kumar, R. Zhang, J.J. De Pablo, M.L. Gardel, Tunable structure and dynamics of active liquid crystals. *Sci. Adv.* **4**, eaat7779 (2018)
12. R.A. Simha, S. Ramaswamy, Hydrodynamic fluctuations and instabilities in ordered suspensions of self-propelled particles. *Phys. Rev. Lett.* **89**, 058101 (2002)
13. Y. Hatwalne, S. Ramaswamy, M. Rao, R.A. Simha, Rheology of active-particle suspensions. *Phys. Rev. Lett.* **92**, 118101 (2004)
14. S. Rafai, L. Jibuti, P. Peyla, Effective viscosity of microswimmer suspensions. *Phys. Rev. Lett.* **104**, 098102 (2010)
15. H.M. López, J. Gachelin, C. Douarche, H. Auradou, E. Clément, Turning bacteria suspensions into superfluids. *Phys. Rev. Lett.* **115**, 028301 (2015)
16. M. Fruchart, C. Scheibner, V. Vitelli, Odd viscosity and odd elasticity. *Annu. Rev. Condens. Matter Phys.* **14**, 471 (2023)
17. L.M. Nash, D. Kleckner, A. Read, V. Vitelli, A.M. Turner, W.T. Irvine, Topological mechanics of gyroscopic metamaterials. *Proc. Natl. Acad. Sci.* **112**, 14495 (2015)
18. M. Brandenbourger, X. Locsin, E. Lerner, C. Coullais, Non-reciprocal robotic metamaterials. *Nat. Commun.* **10**, 4608 (2019)
19. A. Souslov, B.C. Van Zuiden, D. Bartolo, V. Vitelli, Topological sound in active-liquid metamaterials. *Nat. Phys.* **13**, 1091 (2017)
20. G.R. Gossweiler, C.L. Brown, G.B. Hewage, E. Sapiro-Gheiler, W.J. Trautman, G.W. Welshofer, S.L. Craig, Mechanochemically active soft robots. *ACS Appl. Mater. Interfaces* **7**, 22431 (2015)
21. A. Unruh, A.M. Brooks, I.S. Aranson, and A. Sen, Programming motion of platinum microparticles: From linear to orbital. *ACS Appl. Eng. Mater.* (2023)
22. R. Zhang, S.A. Redford, P.V. Ruijgrok, N. Kumar, A. Mozaffari, S. Zemsky, A.R. Dinner, V. Vitelli, Z. Bryant, M.L. Gardel, J.J. de Pablo, Spatiotemporal control of liquid crystal structure and dynamics through activity patterning. *Nat. Mater.* **20**, 875 (2021)
23. I. Buttinoni, G. Volpe, F. Kümmel, G. Volpe, C. Bechinger, Active Brownian motion tunable by light. *J. Phys.: Condens. Matter* **24**, 284129 (2012)
24. S. Li, R. Batra, D. Brown, H.-D. Chang, N. Ranganathan, C. Hoberman, D. Rus, H. Lipson, Particle robotics based on statistical mechanics of loosely coupled components. *Nature* **567**, 361 (2019)
25. M.A. Fernandez-Rodriguez, F. Grillo, L. Alvarez, M. Rathlef, I. Buttinoni, G. Volpe, L. Isa, Feedback-controlled active Brownian colloids with space-dependent rotational dynamics. *Nat. Commun.* **11**, 4223 (2020)
26. S.G. Prasath, S. Mandal, F. Giardina, J. Kennedy, V.N. Murthy, L. Mahadevan, Dynamics of cooperative excavation in ant and robot collectives. *Elife* **11**, e79638 (2022)
27. F. Siebers, A. Jayaram, P. Blümmer, and T. Speck, Exploiting compositional disorder in collectives of light-driven circle walkers. *Sci. Adv.* **9**, eadf5443 (2023)
28. B. Nakayama, H. Nagase, H. Takahashi, Y. Saito, S. Hatayama, K. Makino, E. Yamamoto, T. Saiki, Tunable pheromone interactions among microswimmers. *Proc. Natl. Acad. Sci.* **120**, e2213713120 (2023)
29. N. Aubert-Kato, C. Fosseprez, G. Gines, I. Kawamata, H. Dinh, L. Cazenille, A. Estevez-Tores, M. Hagiya, Y. Rondelez, and N. Bredeche, Evolutionary optimization of self-assembly in a swarm of bio-micro-robots. in *Proceedings of the Genetic and Evolutionary Computation Conference* pp. 59–66 (2017)
30. Z. Zeravcic, V.N. Manoharan, M.P. Brenner, Colloquium: toward living matter with colloidal particles. *Rev. Mod. Phys.* **89**, 031001 (2017)
31. R. Zhang, S.A. Redford, P.V. Ruijgrok, N. Kumar, A. Mozaffari, S. Zemsky, A.R. Dinner, V. Vitelli, Z. Bryant, M.L. Gardel et al., Spatiotemporal control of liquid crystal structure and dynamics through activity patterning. *Nat. Mater.* **20**, 875 (2021)
32. L.M. Lemma, M. Varghese, T.D. Ross, M. Thomson, A. Baskaran, Z. Dogic, Spatiotemporal patterning of exten-

- sile active stresses in microtubule-based active fluids, <https://doi.org/10.1093/pnasnexus/pgad130>. (2022)
33. M. Rubenstein, A. Cornejo, R. Nagpal, Programmable self-assembly in a thousand-robot swarm. *Science* **345**, 795 (2014)
 34. A. Deblais, T. Barois, T. Guerin, P.-H. Delville, R. Vaudaine, J.S. Lintuvuori, J.-F. Boudet, J.-C. Baret, H. Kellay, Boundaries control collective dynamics of inertial self-propelled robots. *Phys. Rev. Lett.* **120**, 188002 (2018)
 35. X. Yang, C. Ren, K. Cheng, H. Zhang, Robust boundary flow in chiral active fluid. *Phys. Rev. E* **101**, 022603 (2020)
 36. A. Dmitriev, A. Rozenblit, V. Porvatov, A. Molodtsova, E. Puhtina, O. Burmistrov, D. Filonov, A. Souslov, N. Olekhno, Statistical correlations in active matter based on robotic swarms. in *2021 International Conference Engineering and Telecommunication (En&T)* (IEEE, 2021) pp. 1–3
 37. L. Giomi, N. Hawley-Weld, L. Mahadevan, Swarming, swirling and stasis in sequestered bristle-bots. *Proc. R. Soc. A: Math. Phys. Eng. Sci.* **469**, 20120637 (2013)
 38. G. Wang, T.V. Phan, S. Li, M. Wombacher, J. Qu, Y. Peng, G. Chen, D.I. Goldman, S.A. Levin, R.H. Austin et al., Emergent field-driven robot swarm states. *Phys. Rev. Lett.* **126**, 108002 (2021)
 39. M. Leyman, F. Ogemark, J. Wehr, G. Volpe, Tuning phototactic robots with sensorial delays. *Phys. Rev. E* **98**, 052606 (2018)
 40. F. Arvin, J. Espinosa, B. Bird, A. West, S. Watson, B. Lennox, Mona: an affordable mobile robot for swarm robotic applications, in *UK-RAS Conference on Robotics and Autonomous Systems* pp. 49–52 (2017)
 41. S.K. Malu, J. Majumdar, Kinematics, localization and control of differential drive mobile robot. *Global J. Res. Eng.* (2014)
 42. J.R. Howse, R.A. Jones, A.J. Ryan, T. Gough, R. Vafabakhsh, R. Golestanian, Self-motile colloidal particles: from directed propulsion to random walk. *Phys. Rev. Lett.* **99**, 048102 (2007)
 43. C. Bechinger, R. Di Leonardo, H. Löwen, C. Reichhardt, G. Volpe, G. Volpe, Active particles in complex and crowded environments. *Rev. Mod. Phys.* **88**, 045006 (2016)
 44. L. Theeyancheri, S. Chaki, N. Samanta, R. Goswami, R. Chelakkot, R. Chakrabarti, Translational and rotational dynamics of a self-propelled Janus probe in crowded environments. *Soft Matter* **16**, 8482 (2020)
 45. J. Tailleur, M. Cates, Statistical mechanics of interacting run-and-tumble bacteria. *Phys. Rev. Lett.* **100**, 218103 (2008)
 46. A.P. Solon, M.E. Cates, J. Tailleur, Active Brownian particles and run-and-tumble particles: a comparative study. *Eur. Phys. J. Special Top.* **224**, 1231 (2015)
 47. H.C. Berg, D.A. Brown, Chemotaxis in *Escherichia coli* analysed by three-dimensional tracking. *Nature* **239**, 500 (1972)
 48. N. Kumar, R.K. Gupta, H. Soni, S. Ramaswamy, A. Sood, Trapping and sorting active particles: motility-induced condensation and smectic defects. *Phys. Rev. E* **99**, 032605 (2019)
 49. L. Angelani, Averaged run-and-tumble walks. *Europhys. Lett.* **102**, 20004 (2013)
 50. V. Balakrishnan, *Elements of Nonequilibrium Statistical Mechanics*, vol. 3 (Springer, 2008)
 51. V. Balakrishnan, On a simple derivation of master equations for diffusion processes driven by white noise and dichotomic markov noise. *Pramana* **40**, 259 (1993)
 52. I. Santra, U. Basu, S. Sabhapandit, Run-and-tumble particles in two dimensions: marginal position distributions. *Phys. Rev. E* **101**, 062120 (2020)
 53. U. Basu, S.N. Majumdar, A. Rosso, G. Schehr, Active Brownian motion in two dimensions. *Phys. Rev. E* **98**, 062121 (2018)
 54. R. Mallikarjun, A. Pal, Chiral run-and-tumble walker: transport and optimizing search. *Physica A* **622**, 128821 (2023)

Springer Nature or its licensor (e.g. a society or other partner) holds exclusive rights to this article under a publishing agreement with the author(s) or other rightsholder(s); author self-archiving of the accepted manuscript version of this article is solely governed by the terms of such publishing agreement and applicable law.